1 GHz Waveform Synthesis With Josephson Junction Arrays

Christine A. Donnelly, Nathan E. Flowers-Jacobs, Justus A. Brevik, Anna E. Fox, *Senior Member, IEEE*, Paul D. Dresselhaus, Peter F. Hopkins, *Senior Member, IEEE*, and Samuel P. Benz, *Fellow, IEEE*

***Abstract*—We synthesize single- and multiple-tone waveforms at gigahertz frequencies from arrays of Josephson junctions and demonstrate their quantum-locked operation over a range of experimental input parameters. We first use a lumped-element circuit to synthesize 1 and 2 GHz single-tone waveforms with −71 dBm output power and in-band spurious-free dynamic range (SFDR) of −66 dBc. We then introduce a narrow-band diplexer circuit and synthesize a 1 GHz sinusoid with higher power (−49 dBm) and in-band SFDR of −79 dBc. To demonstrate the spectrally selective power- and phase-programmability of the diplexer circuit, we also synthesize multisine waveforms with total waveform power of −51 dBm. The spectral purity of the reported waveforms is limited by the room-temperature electronics rather than by the quantized pulse-based synthesis technique. This article provides direction for future circuit designs and uncovers the main factors that must be addressed to achieve higher power, higher spectral purity, and improved output power accuracy. The reported results represent significant progress towards a JAWS-based primary RF reference source that synthesizes programmable, quantum-referenced, low-distortion signals at gigahertz frequencies.**

***Index Terms*—Digital–analog conversion, Josephson junction (JJ) arrays, power measurement, quantization, signal synthesis, superconducting devices, superconducting integrated circuits.**

I. Introduction

THE Josephson arbitrary waveform synthesizer (JAWS) is a superconducting digital-to-analog converter (DAC) [1]–[4] being developed as a primary standard ac waveform source for RF metrology to provide a new, quantum-SI-referenced calibration capability for 4G and 5G communications. Waveform synthesis with JAWS systems has been previously demonstrated at frequencies up to 1 MHz [5] and at amplitudes up to 2 V RMS for a 1 kHz sinewave [6]. Applications of JAWS-synthesized audio-frequency waveforms include calibration of commercial voltage sources [7] and thermal voltage converters [8]; measurement of harmonic distortion, spurious-free dynamic range (SFDR) and noise in commercial electronics [9], [10]; and harmonic phase analysis for distorted waveforms [11], and impedance metrology [12], [13].

To support existing RF power calibration standards and to enable new metrology applications, we are extending JAWS waveform synthesis to gigahertz frequencies [14]. For example, gigahertz JAWS-synthesized waveforms could be used to calibrate the frequency-dependent efficiency of thermistor-based RF power standards and replace the time-consuming process of calorimeter calibration [15]. For this application, an RF-JAWS system would need to supply single-tone power with an uncertainty metric <0.2% at frequencies up to 18 GHz and programmable output power ranging from −30 to 10 dBm [16], where 0 dBm corresponds to 224 mV rms into a 50 Ω load.

A gigahertz RF-JAWS system will also provide a new approach for generating multitone waveforms at selectable relative phases and with power directly referenced to fundamental constants that complements existing sampling and source-based calibration capabilities [17], [18]. For example, JAWS-synthesized multisine waveforms could be used to

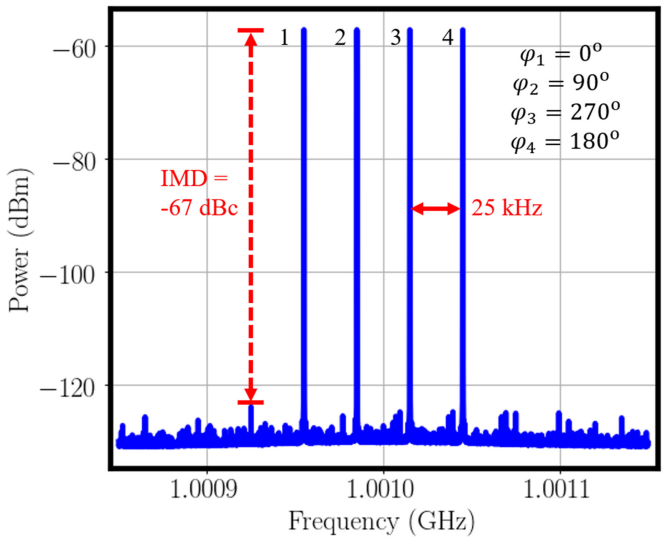

Fig. 1. Demonstration of a four-tone Schroeder-phased multisine signal synthesized using the diplexer JAWS circuit at a center frequency of 1.001 GHz. The individual tones are spaced by 25 kHz, and each has a measured power of −57 dBm. The measurement was performed with a vector signal analyzer with a resolution bandwidth of 100 Hz.

Manuscript received November 16, 2018; revised June 22, 2019; accepted July 16, 2019. Date of publication July 31, 2019; date of current version September 5, 2019. The work of C. A. Donnelly was supported by NIST Graduate Student Measurement Science and Engineering fellowship. This article was recommended by Associate Editor A. Mukhanov. *(Corresponding author: Christine Donnelly.)*

C. A. Donnelly is with the National Institute of Standards and Technology (NIST), Boulder, CO 80305 USA, and also with the Department of Electrical Engineering, Stanford University, Stanford, CA 94305 USA (e-mail: cdonnelly@stanford.edu).

N. E. Flowers-Jacobs, J. A. Brevik, A. E. Fox, P. D. Dresselhaus, P. F. Hopkins, and S. P. Benz are with the National Institute of Standards and Technology (NIST), Boulder, CO 80305 USA.

Color versions of one or more of the figures in this article are available online at http://ieeexplore.ieee.org.

Digital Object Identifier 10.1109/TASC.2019.2932342

calibrate the magnitude and phase response of oscilloscopes and vector signal analyzers; these calibrated electronics are used to characterize leakage between communications channels and nonlinear mixing products in RF communications chains [19], [20]. To be most useful for this purpose, the spectral purity of the RF-JAWS output waveforms must exceed the benchmarks of commercial metrology-grade signal generators: example benchmarks for synthesized signals near 1 GHz include SFDR of -85 to -90 dBc (excluding harmonics and distortion products) and intermodulation distortion (IMD) products of -50 to -55 dBc [21].

As a demonstration of the JAWS system's ability to synthesize gigahertz-frequency signals with calculable spectral power distributions and tunable relative phases, the spectrum of a four-tone (-57 dBm per tone) Schroeder-phased [22] multisine output waveform from one of our RF-JAWS circuits is shown in Fig. 1. The spacing between tones of 25 kHz, which can be made as small as 10 Hz, is close to the subcarrier spacing of 15 kHz used for Orthogonal Frequency Division Multiplexing (OFDM) in Long-Term Evolution (LTE) communications systems [23]. Waveforms with this spacing would also result in improved calibrations compared to frequency combs with 10 MHz minimum tone spacing, or the electro-optic sampling system with a 200 MHz frequency grid [24], which are the main standards currently used at NIST to calibrate the phase response of measurement electronics. The waveform, whose spectrum is shown in Fig. 1, could already be useful for calibrations because it achieves power in each tone that is above the noise floor of the receivers tested with multisine signals in [20], while the largest measured IMD product of -67 dBc is below the distortion level of the receivers in [20]. Future techniques that could improve the spectral purity and increase total waveform power, so that closely spaced tones can be generated with sufficient power per tone over the full-channel bandwidths (1–20 MHz) of LTE systems, is discussed in Section V.

As introduced above, this article demonstrates gigahertz waveform synthesis with two different RF-JAWS circuit designs: a lumped-element JAWS circuit and a bandpass-bandstop (BP-BS) diplexer. Section II provides a general overview of the experimental setup and techniques and demonstrates quantum-locked operation of these circuits. Section III describes the lumped-element JAWS circuit, shows additional experimental results, and presents quantified sources of error in the measured output power. Section IV describes the BP-BS diplexer circuit, shows measured data, and extends the error analysis. Results and future steps are discussed in Section V, and Section VI concludes this article.

II. Experimental Techniques

The JAWS circuit contains an array of superconducting Josephson junctions (JJs) that transform a digitized delta-sigma encoding of a target waveform into an analog sequence of quantized pulses [1], [5]. The digital code is first converted into a pulse sequence by a commercial RF arbitrary waveform generator (RF-AWG) [5]. The AWG signal drives the JJs, which produce the quantized voltage pulses in the JAWS circuit to create the desired output waveform.

The JAWS output pulses are distinguished from the input drive pulses by their quantized time-integrated voltage area of $Nh/2e$, where h is the Planck constant, e is the electron charge, and N is the number of series-connected JJs in the array. When the JAWS circuit is "quantum-locked," each pulse in the input sequence produces one single-flux quantum (SFQ) pulse from each JJ in the JAWS circuit. The average dc output voltage from the quantum-locked JAWS circuit is thus traceable to fundamental constants and is exactly equal to $N\bar{p}h/2e$, where $\bar{p}$ is the average pulse repetition rate. The JAWS circuit is able to maintain error-free, quantum-locked output behavior over non-vanishing ranges of experimental parameter values [25], referred to as the "quantum-locked ranges" of the individual parameters. These experimental parameters include dc bias current, input pulse drive amplitudes, digital filtering parameters for the input code, and environmental variables such as operating temperature. Large quantum-locked ranges are desirable so that the circuit's functional operation is robust with respect to environmental noise and bias variations.

Although audio-frequency JAWS standard reference instruments are operated in cryostats that are refrigerated with a cryocooler and compressor, for the experiments in this article, the RF-JAWS chip is mounted on a cryogenic probe (cryoprobe) and immersed in liquid helium at 4 K. Connections to room-temperature electronics are made using cryogenic-compatible semi-rigid coax for the high-frequency input and output lines. The input pulse signal is generated by a 65×10^9 samples per second Keysight M8195a RF-AWG[1] that has an analog bandwidth of 25 GHz. DC blocks are used to isolate the JAWS chip from low-frequency noise in the input pulse drive. Narrowband (10 MHz bandwidth) bandpass delta-sigma encodings with a maximum pulse repetition rate of 4.8×10^9 pulses per second are used to synthesize the RF-JAWS waveforms, rather than the lowpass encodings used previously for synthesis of 1 MHz and audio frequencies. The digital codes drive SFQ pulses of a single polarity (positive for all waveforms reported in this work), which avoids timing offsets between the positive and negative JJ pulses [26]. The 32-tap finite impulse response (FIR) filter of the RF-AWG is used to shape the input drive pulses [5]. A dc bias current $I_{\rm dc}$ is also applied to the JJs, via either a bias tee at the input to the cryoprobe or by a set of on-chip inductively filtered taps. This dc bias is necessary to achieve and/or test for quantum-locked operation.

Our experiments use arrays of self-shunted, nonhysteretic, and nominally identical JJs with a noninsulating Nb_xSi_{1-x} barrier material and Nb superconducting electrodes. The JJs have critical current $I_C \approx 8$ mA and normal state resistance $R_N \approx 5$ mΩ, corresponding to $I_C R_N \approx 40$ μV. Further details of the experimental procedure, room-temperature electronics, and junction technology are described in [5], [26], [27].

Fig. 2 shows the measurements of the fundamental tone power and integrated in-band noise power vs. $I_{\rm dc}$ for the typical waveforms that are generated by the circuits that will be described in

[1]Commercial instruments are identified in order to adequately specify the experimental procedure. Such identification does not imply recommendation or endorsement by NIST, nor does it imply that the equipment identified is necessarily the best available for the purpose.

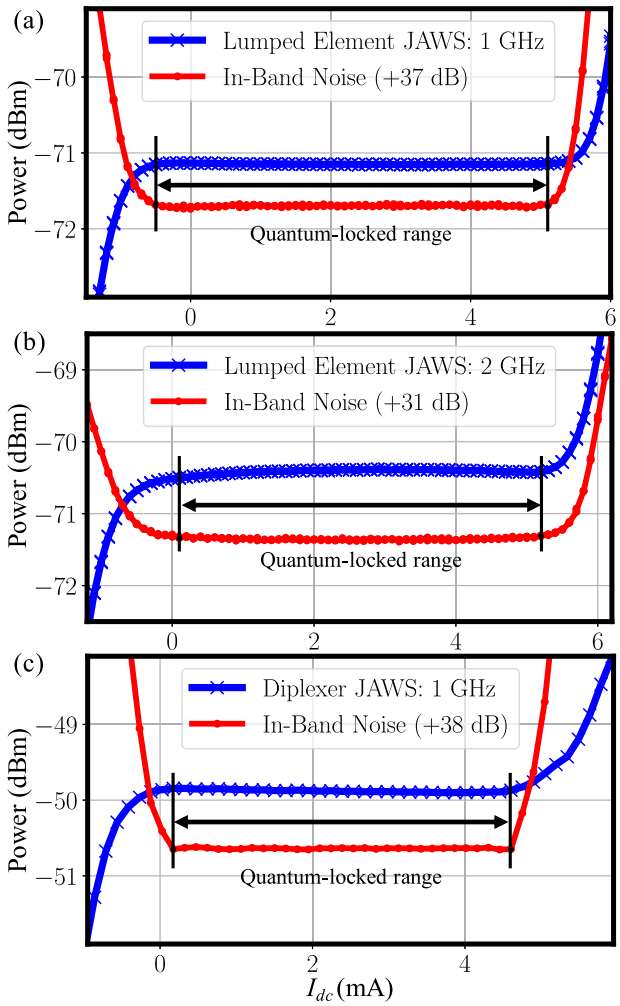

Fig. 2. Measured fundamental tone power and integrated in-band noise power over a 500 kHz bandwidth at 4 K vs. I_{dc} for typical sinusoidal waveforms synthesized at (a) 1 GHz with the lumped-element JAWS circuit, (b) 2 GHz with the lumped-element JAWS circuit, and (c) 1 GHz with the diplexer JAWS circuit. The arrows indicate the range of I_{dc} corresponding to quantum-locked operation for each waveform. A sharper transition is observed in the noise power in (c) compared to (a) and (b) because the background noise power and peak magnitude of the diplexer JAWS circuit are larger than that of the lumped-element JAWS circuit.

this article. Synthesized tones at both 1 and 2 GHz are shown for the lumped-element RF-JAWS circuit, while the narrowband diplexer RF-JAWS circuit design only allows synthesis near 1 GHz. The quantum-locked range (QLR) with respect to I_{dc} is indicated in the figure.

The QLR boundaries shown in Fig. 2 are determined by monitoring two metrics with respect to input parameter values when a particular input pulse drive pattern is applied: (i) the integrated in-band noise power and (ii) the fundamental tone power. The integrated in-band noise power is the most precise metric and was used to determine the QLR with respect to I_{dc} to within ± 0.2 mA for all experiments described in this work. The in-band noise power was determined by integrating the measured power over a 500 kHz bandwidth centered on the fundamental tone and subtracting the power of the fundamental tone. In each panel of Fig. 2, a constant offset was added to the integrated noise for visual comparison to the fundamental tone power. As I_{dc} is swept, the integrated in-band noise decreases to a minimal value when the circuit is quantum-locked. Once the circuit is operating within the QLR, the noise metric remains minimized and invariant with respect to I_{dc} and other input parameters. Specifically, we define the QLR as the range in I_{dc} over which the integrated in-band noise is less than 0.05 dB above the average integrated in-band noise in the center of the QLR.

Next, in test (ii), we measure the fundamental tone power with respect to I_{dc} and determine a region, consistent with the low-noise region of the integrated noise test described above, where fundamental tone power is nearly constant and equal to its programmed value after accounting for sources of error. The measurement of minimal in-band noise power over a range of I_{dc} indicates that the RF-JAWS system is producing an integer number of output pulses in response to each input pulse, but does not confirm that the integer number is equal to one. The synthesized fundamental tone power measurement is an important supplement to the integrated noise power test and is used to confirm that the circuit is locked to the single-pulse output operating regime. Although minor variation in the tone power with respect to I_{dc} is both expected and observed within the QLR at gigahertz synthesis frequencies (as discussed in Section III-D), the dependence of fundamental tone power on I_{dc} is far larger once the circuit is outside of the QLR.

The data in Fig. 2 demonstrate our ability to lock the RF-JAWS circuits to a known operational state that is free of any missing or extra output pulses from one or more junctions. As described above, nonoperational regions outside the quantum-locked range are also observed in Fig. 2, where extra pulses are present (high magnitude of positive I_{dc}) or intended pulses are not synthesized (negative I_{dc}). Even within the quantum-locked range, however, there are multiple sources of error that contribute to a difference between the ideal calculated RF-JAWS output power and the realized output power at the device under test (DUT). We categorize the error contributions into (i) those related to signal transfer from 4 K to 300 K (e.g., cabling losses, reflections at interfaces, and load impedance mismatch); and (ii) those that would be observed at the cryogenic measurement plane. The error contributions in the first category will be corrected by a calibration procedure [28]. This article concentrates on the two main contributions in the second category: (a) "feedthrough," which we define as the residual input drive current signal at the synthesis frequency that reaches the DUT and adds in phase and magnitude to the intentional synthesized signal from the JJs, and (b) the nonzero pulsewidth of the quantized JJ output pulses.

III. Lumped-Element JAWS Circuit

A. Description and Motivation

A schematic of the lumped-element RF-JAWS circuit is shown in Fig. 3. The broadband microwave input pulse drive is terminated on-chip with a 50 Ω resistor that is nominally matched to the input cabling impedance, in series with a short (length 220 μm) array of 102 JJs that is shorted to ground. The array is embedded within the center conductor of a 50 Ω coplanar

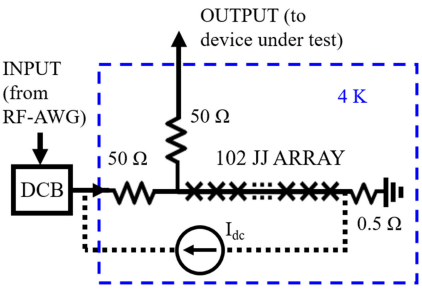

Fig. 3. Schematic of the lumped-element JAWS circuit. The circuit has 50 Ω on-chip resistors in both the input and output paths, and the array of 102 JJs (composed of 34 stacks of 3 JJs each) is shorted to ground with a parasitic resistance of ∼0.5 Ω. The interface between 4 K and room temperature is indicated by the box with dashed lines. A dc block (DCB) is placed at the output of the RF-AWG pulse source.

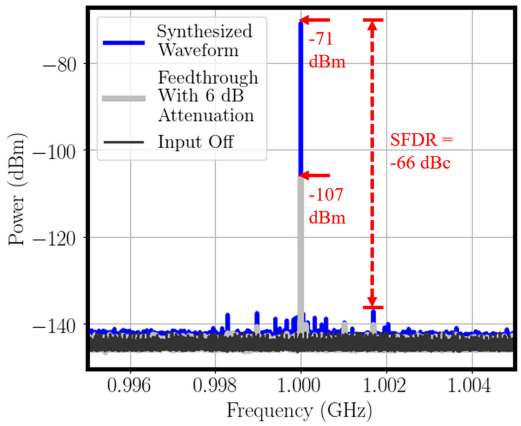

Fig. 4. Measured spectra at 4 K of the synthesized 1 GHz waveform output from the lumped-element JAWS circuit over a 10 MHz range with a 10 Hz resolution bandwidth. The blue data show the spectrum of the synthesized waveform when the circuit is in the quantum-locked range, while the light gray data show the output spectrum "feedthrough" when a 6 dB attenuator is added to the input path. The dark trace shows the output spectrum when all input is turned off, indicating the measurement noise floor.

waveguide (CPW) structure with effective relative permittivity $\epsilon_{rel} \approx 6.0$, such that the array length is less than $\lambda/8$ for all wavelengths λ within the 20 GHz bandwidth of the system ("lumped-element limit"). The output path contains a 50 Ω on-chip resistor that is used to match the low-output impedance of the JJ array to the 50 Ω output cabling and load.

The JJ array can be approximated as an inductive element of less than 100 pH which is dominated by the CPW inductance. The short-circuit to ground is not perfect due to cabling loss and chip contact resistance, resulting in a small additional measured parasitic series resistance of ∼0.5 Ω at 1 GHz between the array and the RF ground. The current from the input pulse drive divides between the path to ground through the JJ array and the 50 Ω output path to the DUT, substantially reducing feedthrough to the DUT at the 1 GHz synthesis frequency.

B. Demonstration of 1 GHz Synthesis

Fig. 4 shows the spectrum of a 1 GHz waveform synthesized with the lumped-element JAWS circuit over the 10 MHz bandwidth of the input delta-sigma code. The output waveform spectrum was measured with a vector signal analyzer using a 10 Hz resolution bandwidth. The vector signal analyzer has a specified uncertainty of ±0.28 dB in measured power at 1 GHz and an uncertainty of ±2° in measured phase. Two other spectra are also shown in Fig. 4: (a) the measurement noise floor when the input drive is turned OFF and (b) the measured feedthrough when the input drive is present but intentionally attenuated by 6 dB and $I_{dc} = 0$ to prevent the JJs from producing any SFQ output pulses. Under these input conditions, the feedthrough signal at the synthesis frequency is −107 dBm.

Fig. 4 also shows that the power of the synthesized tone is −71 dBm and the SFDR is −66 dBc. The largest spurs at full input amplitude are all observed in the feedthrough spectrum, taking into account the noise floor and 6 dB attenuation. The spectral purity is thus limited by feedthrough from spurious content in the input pulse drive.

Input pulse-shaping techniques were required to reduce feedthrough to the level observed in Fig. 4. In the absence of any pulse-shaping techniques, the feedthrough from the input drive signal at 1 GHz was −33 dBm. To reduce this unwanted contribution to the output waveform, we first used the "zero-compensation" technique described in [5] to shape, and effectively high-pass filter, the individual input drive pulses. Because JJs are nonlinear devices, they can synthesize a given frequency even when it has been completely removed from the input drive. With the zero-compensation pulse shape as a baseline, we then performed an additional optimization routine by varying the RF-AWG FIR tap values to minimize feedthrough at the synthesized tones. The optimization routine was repeated with each thermal cycle of the JAWS circuit because the feedthrough signal is sensitive to factors such as temperature-dependent output cabling attenuation and probe-to-chip contact resistance.

C. Effect of Feedthrough on Signal Accuracy

We combine the measured feedthrough due to the attenuated input pulse drive with SPICE [29] simulations of the JJ array to correct for the contribution of the feedthrough to the output power in the quantum-locked range. With 6 dB of attenuation in the lumped-element circuit input path, the input pulse drive creates a 1 GHz signal due to (i) synthesis of a small 1 GHz signal $V_{\mathrm{JJ,att}}$ due to the zero-voltage area output response from the JJs to each attenuated input pulse, (ii) a voltage drop $I_{\mathrm{inp,att}} Z_{\mathrm{array}}$ of the attenuated 1 GHz input component $I_{\mathrm{inp,att}}$ across the linear part of the array impedance Z_{array} (a fixed CPW inductance in series with the 0.5 Ω contact resistance to ground), and (iii) a voltage drop $I_{\mathrm{inp,att}} Z_{\mathrm{JJ}}$ of the 1 GHz input component across the nonlinear, input-pulse-magnitude-dependent impedance of the JJs in the array Z_{JJ} (a variable inductance in the small-signal model) [30], [31]. All terms defined in Section III-C refer to the $f = 1$ GHz component of frequency-domain functions, although the repeated ($f = 1$ GHz) notation is omitted for readability. The combination of terms (ii) and (iii) constitutes the 1 GHz feedthrough signal from the input pulse drive, while term (i) is a nonlinear frequency-generation effect that is present even if $I_{\mathrm{inp,att}}$ (at $f = 1$ GHz) is equal to zero.

After combining terms (i) through (iii), the output voltage $V_{\rm att}$ at 1 GHz with 6 dB of input attenuation is given by

$$V_{\rm att} = V_{\rm JJ,att} + I_{\rm inp,att}(Z_{\rm array} + Z_{\rm JJ}). \quad (1)$$

When the input drive is increased by 6 dB to full scale ($I_{\rm inp}$), it similarly creates a 1 GHz signal that is the sum of (i) the desired quantized output waveform $V_{\rm JJ}$, (ii) $I_{\rm inp}Z_{\rm array}$, and (iii) a voltage drop across the nonlinear impedance of the JJs under full-scale input, $I_{\rm inp}Z_{\rm JJ}$ [31]. This full-scale output voltage $V_{\rm full}$ is thus given by

$$V_{\rm full} = V_{\rm JJ} + I_{\rm inp}(Z_{\rm array} + Z_{\rm JJ}). \quad (2)$$

Again, the second and third terms constitute the feedthrough signal when $I_{\rm inp}$ is nonzero. The first term is generated by the JJs at $f = 1$ GHz even when $I_{\rm inp}$ is equal to zero. As long as the linear feedthrough terms involving $Z_{\rm array}$ dominate over all other terms besides $V_{\rm JJ}$, the 1 GHz signal (as measured with 6 dB input attenuation) simply increases by 6 dB when the attenuation is removed and can be subtracted as a feedthrough correction factor from the full-scale output in order to isolate the desired signal $V_{\rm JJ}$. Using this approximation, the JJ-synthesized output power is given by

$$\frac{V_{\rm JJ}^2}{Z_0} \approx \frac{\left[V_{\rm full} - \alpha^{-1}V_{\rm att}\right]^2}{Z_0} \quad (3)$$

where α is the (linear) attenuation factor and is nominally equal to 0.5 (-6 dB), and Z_0 is the characteristic impedance of the output load. Both magnitude and relative phase of the terms in (3) are important for an accurate feedthrough correction. For the lumped-element circuit, the linear feedthrough signal is in quadrature with $V_{\rm JJ}$ if the array impedance is purely inductive; parasitic resistance in the path to ground and capacitive coupling between the input and output lines decrease the relative phase between the two signals.

Based on simulations of the lumped-element circuit JJ array that include the transmission-line properties, the nonlinear impedance $Z_{\rm JJ}$ is confirmed to be small ($<$10%) relative to $Z_{\rm array}$ at 1 GHz, at both input amplitudes and at all $I_{\rm dc}$ within the quantum-locked range. The contribution to the feedthrough signal of $Z_{\rm JJ}$ will increase relative to $Z_{\rm array}$ if arrays with more densely spaced JJs (i.e., more JJs per stack) or JJs with lower I_C (i.e., larger Josephson inductance) are used in the future. In contrast, $V_{\rm JJ,att}$ is significant at 1 GHz ($\sim$25% of $I_{\rm inp,att}Z_{\rm array}$) and adds as much as 1.5 dB to the measured output power with the 6 dB of input attenuation, thus impacting the linear feedthrough scaling assumption in (3). The relative contribution of $V_{\rm JJ,att}$ will further increase if input codes with denser pulse spacing, intended to synthesize higher power waveforms, are used in the future.

After correcting for the phase shift of the attenuator, the signal $V_{\rm att}$ has a measured phase of 53° relative to $V_{\rm full}$ at the center of the quantum-locked range. After also accounting for the actual value of α (as measured with a vector network analyzer) and the simulated contributions (both magnitude and phase) of the nonlinear terms not included in (3), we determine that feedthrough creates an approximately +4% error between the measured power and the programmed JJ-synthesized power at 1 GHz in the center of the quantum-locked range. Multiple sources of uncertainty are involved in determining this error correction factor, and the best way to reduce uncertainty will be to change the circuit to reduce the magnitude of $I_{\rm inp}$ at 1 GHz.

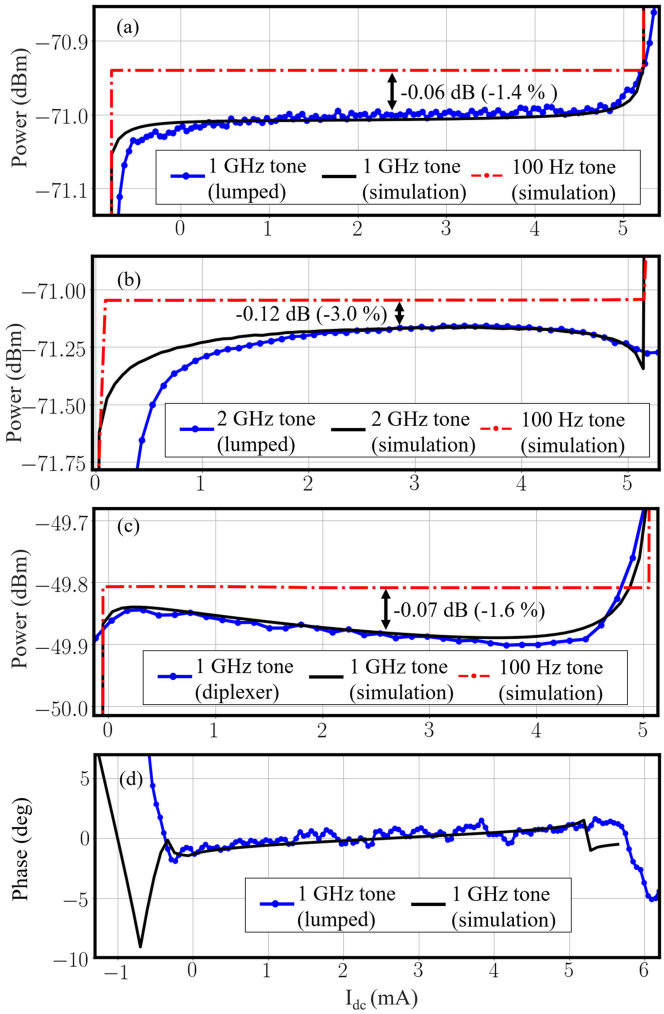

Fig. 5. Measured variation at 4 K of the fundamental tone power (connected circles) and the calculated variation using a SPICE simulation (solid curves) as a function of dc offset current $I_{\rm dc}$. The curves are shown for (a) 1 GHz synthesis with the lumped-element circuit, (b) 2 GHz synthesis with the lumped-element circuit, and (c) 1 GHz synthesis with the diplexer circuit. The simulated dependence of fundamental tone power on $I_{\rm dc}$ at $f = 100$ Hz is also shown for all circuit configurations, to confirm that the variation in power over the quantum-locked range (QLR) is not present for low-frequency synthesis. Finally, the measured variation in the synthesized signal phase over the QLR for 1 GHz synthesis with the lumped-element circuit is shown in (d) and is compared to the simulation result.

D. Dependence of Synthesized Tone Power on I_{dc}

Fig. 5(a) and (b) shows the fundamental tone power vs. $I_{\rm dc}$ for waveform synthesis with the lumped-element circuit at 1 and 2 GHz, respectively, measured at 4 K. These data and the QLR data shown in Fig. 2(a) and (b) were not taken simultaneously and the system was thermally cycled between the data runs. Fig. 5(c) shows the fundamental tone power vs. $I_{\rm dc}$ for the diplexer circuit at 1 GHz and is the same data, but on a magnified y-axis scale, as shown in Fig. 2(c). The diplexer circuit will

be discussed in detail in Section IV. Fig. 5(a)–(c) reveals a small variation in the measured fundamental tone output power as a function of $I_{\rm dc}$. Fig. 5(d) shows a linear trend in the lumped-element circuit 1 GHz signal phase vs. I_{dc} over the quantum-locked range, with a slope of $\sim 0.5^{\circ}/\text{mA}$.

The trend in phase can be explained by an $I_{\rm dc}$-dependent timing shift in the triggering of SFQ pulses by the input drive and maps to a pulse phase delay at 1 GHz of 1.5 ps/mA [26]. We quantitatively interpret the trend in synthesized signal power based on variation in the shape of the SFQ pulses themselves as a function of $I_{\rm dc}$. We call the net pulse shape (i.e., the summation of the individual SFQ pulses from all N JJs in the array) $p(t)$, with one pulse $p(t)$ produced for each "1" in the input delta-sigma code. In the lumped-element limit, $p(t)$ is indistinguishable from an SFQ pulse produced by a single JJ, with amplitude multiplied by N. Mathematically, the output synthesized waveform $v_{\rm JJ}(t)$ is expressed as

$$v_{\rm JJ}(t) = p(t) \otimes \sum_n w[n]\delta(t - nT) \tag{4}$$

where t refers to time, $w[n]$ is the input delta-sigma code bitstream indexed by "n," $\otimes$ is the convolution operator, T is the clock period of the delta-sigma code, and $\delta(t)$ is the Kronecker delta function (here used to translate the digital code into the time domain via the clock period).

The analog for (4) in the frequency domain is

$$V_{\rm JJ}(f) = P(f)W(f) \tag{5}$$

where $V_{\rm JJ}(f)$, $P(f)$, and $W(f)$ are the Fourier transforms of the output synthesized waveform $v_{\rm JJ}(t)$, net quantized pulse $p(t)$, and input delta-sigma code $w(t)$, respectively. Because the time integral of $p(t)$ is quantized, the dc component of $P(f)$ [i.e., $P(0)$] is exactly known. However, because $p(t)$ has a nonzero pulsewidth, the value of $P(f)$ the value of $P(f)$ deviates from $P(0)$ typically for frequencies f near 1 MHz and above [32]. Moreover, $p(t)$ varies based on the value of $I_{\rm dc}$ even while maintaining its quantized integral, which causes $P(f)$ to be dependent on $I_{\rm dc}$ at all frequencies besides $f = 0$ [26]. These effects are simulated to contribute <0.0001% (1 ppm) variation in output power over the quantum-locked range for 1 MHz synthesis using JJs with $I_C R_N = 40$ μV and were thus not observed for waveforms synthesized at 1 MHz [5].

We used SPICE simulations of SFQ pulses to show that the measured variation in waveform power at 1 and 2 GHz seen in Fig. 5(a)–(c) can be attributed to changes in $P(f)$ with $I_{\rm dc}$. The SPICE simulations used the resistively shunted junction (RSJ) model [30] to approximate the JJ dynamics and solve for the time-domain behavior of the lumped-element circuit under input pulse excitation.

To determine the input pulses used in the simulations, we measured time traces of the optimized input pulses with a sampling oscilloscope at the input to the cryoprobe. We also measured the scattering parameters (S parameters) of the cryoprobe cabling from room-temperature input to the 4 K JAWS chip, using an on-chip through-line structure and assuming symmetry in the paths from probe input to chip and from chip to probe output. The measured input pulses were transferred (in simulation) through the measured S parameters. For the purpose of diplexer circuit simulations shown in Fig. 5(c), the input pulses were also transferred through the measured S parameters of a bandstop filter that is located on-chip.

Next, in simulation, we used the input pulses to drive SFQ pulses from series-connected arrays of JJs with $I_C R_N = 40$ μV at a range of $I_{\rm dc}$ and recorded the simulated magnitude of $P(f = 1\text{ GHz})$ and $P(f = 2\text{ GHz})$ as a function of $I_{\rm dc}$. The input pulse amplitudes and value of JJ I_C were left as simulation-fitting parameters. A fitted value of $I_C = 8$ mA was used for the lumped-element circuit simulations, and $I_C = 8.5$ mA was used for the diplexer circuit simulations. In addition, an overall $I_{\rm dc}$-independent attenuation was fitted to the simulated magnitude of $P(f)$ in order to account for experimental attenuation between the JAWS chip and the measurement electronics. The value of $W(f)$ at 1 and 2 GHz was constant, as determined by the fast Fourier transform (FFT) of the digital code amplitude. The resulting simulated dependence on $I_{\rm dc}$ of RF power $|V_{\rm JJ}(f)|^2/Z_0 = |P(f)W(f)|^2/Z_0$ is shown in Fig. 5(a) and (c) for 1 GHz synthesis with the lumped-element and diplexer circuits, respectively, and is shown in Fig. 5(b) for 2 GHz synthesis with the lumped-element circuit. All simulated dependence of RF output power on $I_{\rm dc}$ is due to the change in $P(f)$ with $I_{\rm dc}$. The simulations agree well with the experimental data at both frequencies and for both circuit designs. The simulation of phase variation in $P(f)$ with respect to $I_{\rm dc}$ for 1 GHz synthesis with the lumped-element circuit also agrees well with experimental data within the QLR, as shown in Fig. 5(d). The simulations did not include the effects of JJ I_C nonuniformity, thermal noise, deviation in the actual JJ behavior from the RSJ model, or error in the S parameter measurements that were used to determine the simulated input pulse shape; all of these factors may have caused imperfect agreement between simulation and measurement.

At all values of $I_{\rm dc}$ within the quantum-locked range, the value of $P(f)$ is less than the known value of $P(0) = Nh/2e$. To further illustrate this point, Fig. 5(a)–(c) also shows the simulated magnitude of output power $|P(f)W(f)|^2/Z_0$ when $f = 100$ Hz, which is essentially equal to the calculable value of power at $f = 0$. The difference between the low-frequency and RF simulation curves is fully attributable to rolloff in $P(f)$ at higher frequencies because the simulations for $f = 100$ Hz used the same overall attenuation offset values, input pulse shapes and values of I_C and $I_C R_N$ as the simulations described above. With the input pulse shape used in our experiments, there is a simulated discrepancy between programmed and realized output power of $\left[|P(f)|^2 - |P(0)|^2\right]/|P(0)|^2 = -1.4\%$ at the center of the quantum-locked range for the lumped-element circuit at 1 GHz, and a discrepancy of -1.6% for the diplexer circuit at 1 GHz. At 2 GHz, the simulated difference at the center of the QLR increases to -3.0%. The loss can be reduced by increasing the $I_C R_N$ of the JJs and decreasing the effective width of the input pulses and does not represent a fundamental physical limitation on the frequency or accuracy of JAWS-based waveform synthesis.

E. Overall Error Accounting

The demonstrated 1 GHz waveform with -71 dBm measured power was synthesized from a code intended to produce

−68.2 dBm power at 1 GHz. Most of this −2.8 dB loss is explained by off-chip measurement components, including (i) SMA cabling attenuation (contributing 1–1.5 dB overall loss) and (ii) attenuation at the signal analyzer input or miscalibration of the signal analyzer (up to 2 dB loss, based on a similar test of the measurement loss for a room-temperature programmable signal generator). While these off-chip loss contributions are large in magnitude, they are specific to our current test infrastructure. Once the final packaging of the RF-JAWS system is established, a low-uncertainty S-parameter calibration procedure will be performed for every component in the measurement chain so that the plane of measurement is transferred back to the JAWS chip [28], [33].

The two main identified error contributions that are intrinsic to the circuit design and junction technology have been discussed in detail: the measured error due to feedthrough contributes approximately +0.2 dB error between programmed and measured power with the lumped-element circuit at the center of the quantum-locked range, while the non-zero quantized JJ voltage pulsewidth contributes a simulated −0.06 dB error at 1 GHz and a −0.12 dB error at 2 GHz. An additional source of error that has not been discussed in this article will include power loss from the quantized synthesized pulses due to the impedance of the other JJs in the array (Z_{JJ}); this source of loss will increase in magnitude for longer arrays or higher synthesis frequencies but is still negligible (<0.01 dB) for the circuits and frequencies described in this work.

F. Limited Circuit Output Power

For short JJ array lengths, the lumped-element JAWS circuit features a nearly ideal on-chip 50 Ω termination for the input microwave pulse drive. This favorable microwave property makes it straightforward to find FIR tap parameters that result in quantum-locked operation, and there is a wide parameter space available to optimize the input pulses for feedthrough minimization.

However, for synthesis of waveforms with higher power, the array length will need to be increased beyond the lumped-element limit to accommodate more JJs. In this case, the array will act as a shorted transmission line stub, and the resulting standing waves will lead to nonuniformity in the pulse drive such that all the JJs will not be simultaneously quantum-locked to the pulse drive. Simulations indicate a length of 2.4 mm (1120 JJs using the current fabrication technology) as an upper limit; for longer arrays, reflections will cause the input pulse amplitude to vary by >30% over the length of the array, assuming a ∼50 ps input pulsewidth. This prevents quantum-locked operation with any input pulse amplitude. Therefore, this single lumped-element JAWS circuit is only intended for use in low-power applications.

IV. Bandpass-Bandstop Diplexer JAWS Circuit

A. Description and Motivation

For waveform synthesis with longer arrays of JJs, the array must be terminated in a matched 50 Ω impedance rather than shorted to ground. This requirement exacerbates the feedthrough problem, because it is no longer possible to prevent input current from reaching the measurement load by shorting the current through the small array impedance.

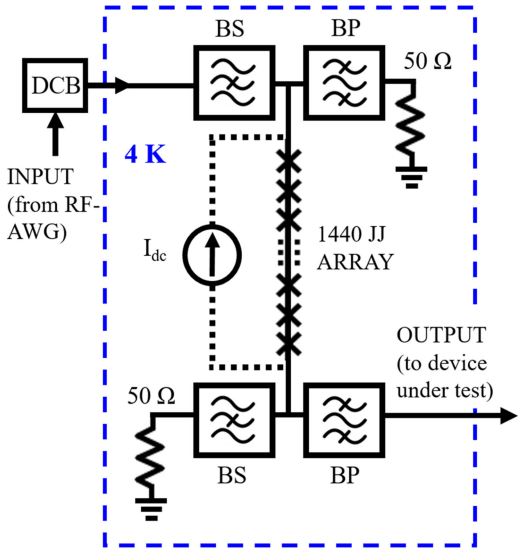

Fig. 6. Schematic of the bandpass-bandstop diplexer JAWS circuit. Identical diplexer filter structures are located above (input) and below (output) the array of JJs. All filters are 1 GHz bandpass (BP) or bandstop (BS). The interface between 4 K and room temperature is indicated by the box with dashed lines. As with the lumped-element circuit, a dc block (DCB) is placed between the RF-AWG pulse source and the cryogenic probe input.

A new circuit, designed for synthesizing 1 GHz waveforms and called the "bandpass-bandstop (BP-BS) diplexer RF-JAWS," addresses these challenges and is shown schematically in Fig. 6. This circuit uses 1440 JJs connected in series, increasing the number of JJs by more than an order of magnitude compared to the lumped-element circuit.

The BP-BS diplexer RF-JAWS chip contains a set of back-to-back three-port diplexer structures [34]–[36]. The JJ array is located between the diplexers and is connected to the composite port of both diplexers. Each diplexer consists of a parallel combination of 1 GHz bandpass and bandstop filters, so that microwaves leaving either end of the JJ array ideally encounter a frequency-independent 50 Ω termination. The input bandstop filter (upper left in Fig. 6) reduces feedthrough error by filtering the 1 GHz component in the input pulse drive. The forward-propagating half of the synthesized waveform is measured on the 1 GHz bandpass output filter port (bottom right of Fig. 6), where the bandpass filter reduces out-of-band measurement feedthrough. The back-propagating half of the synthesized waveform is terminated on-chip by the input bandpass filter (upper right in Fig. 6). The circuit output captures only the forward-propagating portion of each JJ pulse, allowing the circuit to be scaled to longer array lengths and higher synthesis frequencies by avoiding the time-of-flight pulse broadening associated with the backward traveling JJ pulses [37].

The bandpass and bandstop filters use superconducting lumped-element passive components with values based on singly terminated, second-order Butterworth filter design principles [38]. The stopband and passband of the bandstop and

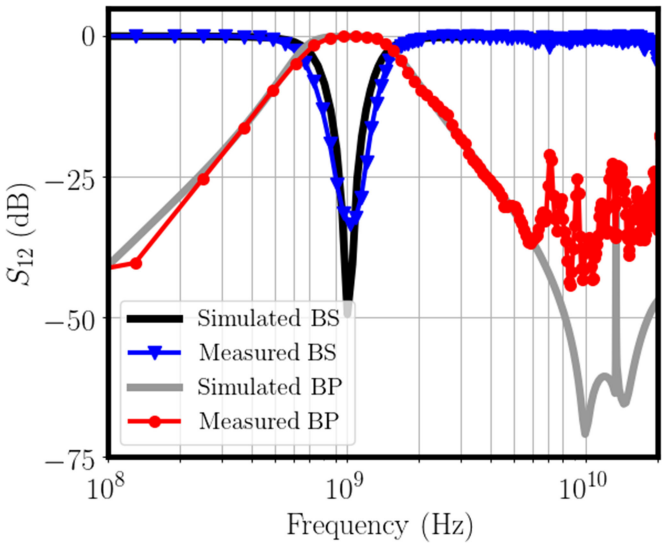

Fig. 7. Simulated (black and gray curves without markers) vs. 4 K measured (blue and red curves with triangles and circles) values of S_{12} for the fabricated bandstop (BS) and bandpass (BP) diplexer filters over the full 20 GHz system bandwidth. Prior to the measurements, a transmission calibration was performed using an on-chip coplanar waveguide through-line structure.

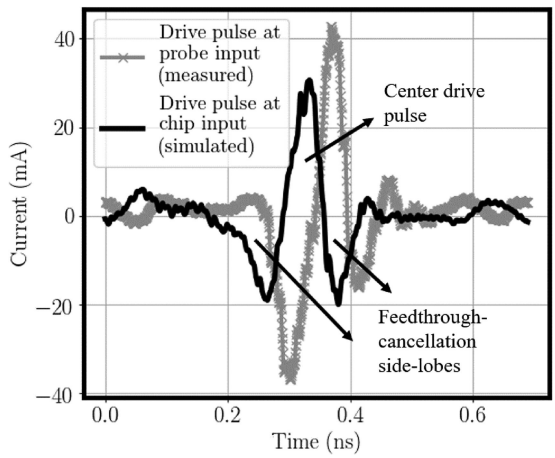

Fig. 8. Input bias pulses used to drive SFQ pulses from the diplexer JAWS circuit array, as measured at the input to the cryogenic probe (light curve) and as transformed in simulation to the JAWS array input (dark curve). The black pulse shape is close to the desired "zero-compensation" input pulse shape.

bandpass filters, respectively, are narrow (∼800 MHz) relative to the 20 GHz input code bandwidth so that the majority of the input code frequency content passes through the input bandstop filter, through the JJ array to drive SFQ pulses, and through the output bandstop filter to the on-chip termination (bottom left of Fig. 6).

B. Microwave Design and Verification

Prior to fabrication, the diplexer was designed and simulated with a commercial microwave software package. The simulated values of transmission S parameter S_{12} for the bandpass and bandstop filters comprising the diplexer are shown in Fig. 7. The values of S_{12} for both filters were measured at 4 K and are also shown in Fig. 7. Overall, the input bandstop filter reduces feedthrough at 1 GHz by 40 dB, which is comparable to the feedthrough reduction inherent in the lumped-element JAWS design. The filter S parameters were measured using on-chip diplexer test structures that contained no JJs. For these measurements, a transmission calibration was performed for the vector network analyzer using an on-chip through-line structure. The small discrepancy between microwave simulation and measurement can be explained by circuit parasitics that cause the filter termination impedances to deviate from their nominal value of 50 Ω, as well as differences between targeted and actual fabrication parameters (e.g., dielectric layer thickness). For example, a fabrication offset from the target dielectric thickness of +10% (or an offset from the assumed dielectric constant of –10%) would explain both the reduced notch depth in the measured bandstop filter S_{12} relative to the microwave simulation and the slight offset of the notch minimum from 1 GHz. At frequencies above 5 GHz, inaccuracy of the through-line calibration technique likely also contributes to the observed oscillation in the bandpass filter S_{12}. For future RF-JAWS circuits, we plan to fabricate on-chip the through, reflect, line (TRL) elements necessary for calibrating signals at the RF-JAWS chip for improved high-frequency measurement of S parameters.

C. Achieving Quantum-Locked Operation

The nonlinear phase of the bandstop filter in the microwave input path changes the shape of the input pulses. Therefore, unlike with the lumped-element circuit, quantum-locked circuit operation could not be achieved for the BP-BS circuit by making small modifications to a simple bipolar input pulse shape [5].

Instead, the RF-AWG FIR taps were used to correct for the frequency and phase response of the diplexer filter. We first measured the S parameters of the probe-to-chip cabling and input bandstop filter using the methods discussed in Sections III-D and IV-B, respectively. In a standard predistortion procedure, we divided the FFT of the desired pulse by S_{12} for the overall frequency-dependent input path and took the inverse FFT to determine the input pulse shape needed to produce the desired pulse shape on-chip. The necessary input pulse shape was realized with the RF-AWG FIR taps.

Fig. 8 shows the drive pulse measured at the input to the cryoprobe and the simulated drive pulse at the input to the JJ array. The simulated pulse shape is close to the targeted zero-compensation pulse, containing a larger positive center lobe to drive SFQ pulses and two smaller negative sidelobes which effectively high-pass filters the input pulses and reduces feedthrough at the synthesis frequency.

We achieved quantum-locked behavior over a 3.4 mA bias range by using this predistortion technique to shape the input pulses. A quantum-locked range of this magnitude exceeds our target minimum range and ensures stable circuit operation even if significant environmental fluctuations in I_{dc} occur.

D. Effect of Feedthrough on Signal Purity and Accuracy

The spectrum of a 1 GHz waveform synthesized with the bandpass-bandstop diplexer RF-JAWS circuit is shown in Fig. 9

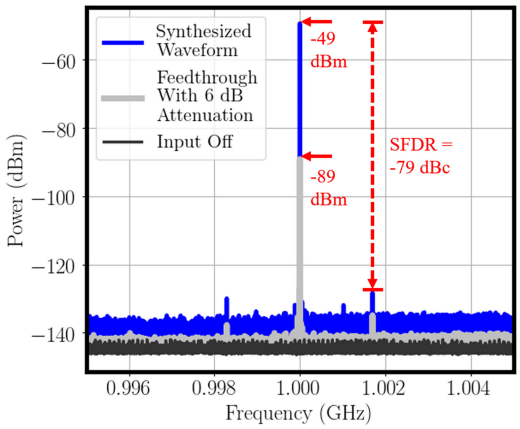

Fig. 9. Measured spectra at 4 K of a 1 GHz synthesized waveform output from the diplexer JAWS circuit over a 10 MHz range with a 10 Hz resolution bandwidth. The blue data show the spectrum of the synthesized waveform when the circuit is in the quantum-locked range, while the gray data show the output spectrum when a 6-dB attenuator is added to the input path. The dark trace shows the measured output when all input is turned OFF, indicating the measurement noise floor.

over the 10 MHz bandwidth of the input delta-sigma code. Two other spectra are also shown: (i) the measurement noise floor when the input waveform is turned OFF and (ii) the measured feedthrough when the input drive waveform is present but attenuated by 6 dB to prevent the JJs from producing quantized pulses. The synthesized signal is measured at −49 dBm, and the feedthrough signal at the fundamental tone is measured to be −83 dBm after accounting for the 6 dB attenuator and the other factors discussed in Section III-C. The in-band feedthrough power with the diplexer circuit is higher than that of the lumped-element circuit because the FIR tap values are constrained by the predistortion routine and therefore cannot be optimized to solely minimize feedthrough.

We measure a relative phase of 18° between the synthesized signal and the feedthrough, which is smaller than the relative phase measured for the lumped-element circuit. In the case of the lumped-element circuit, the feedthrough signal is generated across the JJ array inductance and other parasitic components in the ground path. With the diplexer circuit, in contrast, both the input drive signal and synthesized waveform are transmitted in phase to the output load. The residual nonzero phase offset between the signals is due to phase shift of the 1 GHz component of I_{inp} introduced by the FIR filtering and on-chip bandstop filter, neither of which affects the synthesized waveform.

Despite larger feedthrough magnitude and smaller phase angle compared to the lumped-element circuit, the diplexer circuit contains more JJs and the synthesized signal is larger so the fractional error in output power due to feedthrough is comparable (4%) between the two circuits. Further improvement in signal-to-feedthrough ratio should be possible with longer arrays (more JJs), because the synthesized waveform power will increase but the input drive power and resulting feedthrough will remain the same.

The in-band feedthrough with the diplexer circuit includes densely spaced spurious tones at the input code repetition frequency (50 Hz) that rise above the measurement noise floor. This spurious feedthrough content from the input pulse drive limits the SFDR to −79 dBc. We have not yet been able to remove this feedthrough to measure the inherent SFDR of the raw waveform synthesized by the JJs.

E. Overall Error Accounting and Error Linearity

The demonstrated waveform with −49 dBm measured power at 1 GHz was synthesized from a code intended to produce –46.1 dBm power at 1 GHz. Most of this −3.3 dB loss is explained by off-chip measurement components that are discussed in Section III-E. The output cabling loss is temperature-dependent and varies based on the helium level in the 4 K measurement setup, which can explain the additional 0.5 dB of loss observed with the diplexer circuit relative to the lumped-element circuit. With the diplexer circuit, feedthrough contributes an error of +0.09 dB between the programmed and measured power, while the nonzero pulsewidth of the quantized pulses contributes approximately −0.06 dB error (assuming a similar input pulse shape to the lumped-element circuit after accounting for predistortion).

The diplexer circuit has higher dynamic range than the lumped-element circuit, and it was thus possible to measure the output power discrepancy at a range of programmed powers, with results shown in Fig. 10(a). The input-to-output power transfer function in Fig. 10(a) follows a linear curve with unity slope and a constant offset of −3.2 dB. (These data were taken during a separate thermal cycle relative to the data in Fig. 9.) The deviation in the curve from a linear fit is shown in Fig. 10(b), with error bars indicating the standard deviation at each data point after 12 repeated measurements. Verifying the linearity of the RF-JAWS system (to within measurement capabilities) is an important step towards synthesizing multitone signals with programmable power ratios that are traceable to fundamental constants. Traceability of the absolute power levels will be achieved by calibrating the system to the JJ array using an on-chip calibration kit, which will remove the constant offset seen in Fig. 10(a).

V. Discussion and Future Steps

Near-term goals for gigahertz waveform synthesis with the RF-JAWS system include (i) achieving higher output power (at least −30 dBm), (ii) improving SFDR and reducing error in the output power by reducing feedthrough, (iii) reducing loss in output power due to dependence of $P(f)$ on frequency, and (iv) synthesizing higher output frequencies.

Higher output power can most easily be achieved by increasing the number of series-connected JJs in the diplexer circuit array. Unlike the lumped-element circuit, whose length is limited by impedance mismatch, the upper limit to the array length of the diplexer circuit is reached when microwave attenuation along the length of the array (due to finite R_N of the JJs) makes it impossible to drive SFQ pulses. Previous experiments and simulations of JAWS circuits designed for lower synthesis frequencies indicate that we will be able to increase the number of JJs in the single series-connected array to at least 6000, corresponding to an output power of about –37 dBm. In addition, the waveforms reported here were synthesized from delta-sigma codes with at least five time steps between positive

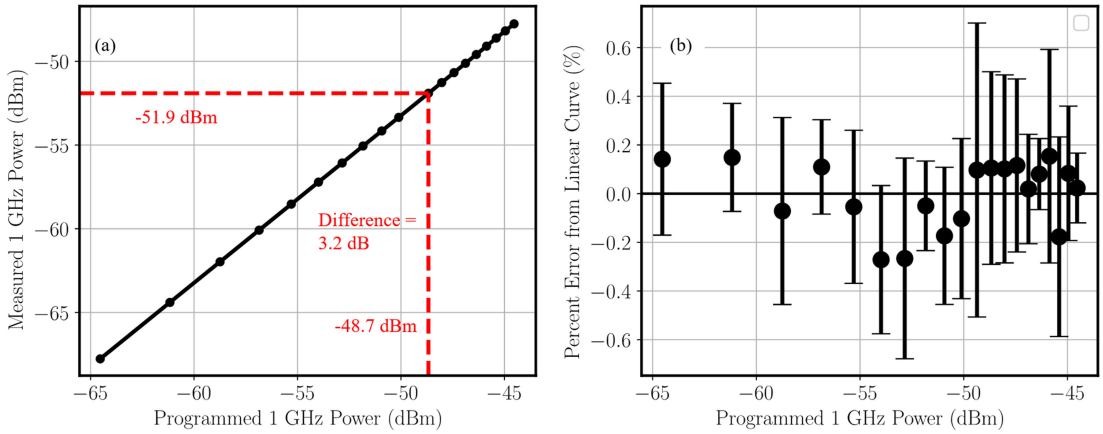

Fig. 10. (a) Programmed vs. measured output power for 1 GHz synthesis with the BP–BS diplexer circuit at 4 K. The curve is linear with a unity slope and a constant difference of 3.2 dB at each data point. (b) Percentage deviation of the curve in (a) from a perfect line with unity slope. The mean values from 12 repeated measurements are shown, and the error bars show the standard deviation of the measurement at each data point.

pulses, that is, at a maximum pulse repetition rate of 4.8×10^9 pulses per second, in order to minimize overlap of adjacent input drive pulses that causes nonuniform input pulse shapes and degrades the quantum-locked range. For comparison, low-frequency <1 MHz waveforms are typically encoded with a maximum pulse repetition rate of 14.4×10^9 pulses per second [6]. If the pulse repetition rate of the GHz waveforms can be doubled while avoiding input pulse overlap, the target output power of nearly –30 dBm will be achieved. To further increase output power by increasing the number of JJs, we could drive multiple arrays in parallel and add their outputs using a power combiner. However, this technique will introduce additional sources of error.

Feedthrough from the input source, which contains power not only at the fundamental tone but also at spurious frequencies, is particularly undesirable because it limits the accuracy of the fundamental tone output power and also degrades SFDR. To address this problem, we will design a higher order diplexer bandstop filter with higher stopband attenuation. For example, simulations show that a fourth-order filter design will increase stopband attenuation to 80 dB, even when expected process variations are included in simulations. The stopband attenuation of the bandpass filter is also a key parameter for calibrating RF power detectors, which are not frequency-selective and measure all incident power. Higher order filters will also improve the bandpass filter performance.

To reduce the effect of nonideal pulse frequency response $P(f)$ on the RF-JAWS output waveform power and phase, we intend to fabricate JJs with higher values of $I_C R_N$, corresponding to narrower pulsewidths. Simulations indicate that the error due to nonzero pulsewidth will be reduced by at least a factor of two if $I_C R_N$ is increased to 80 μV, although the quantum-locked range will decrease unless the input drive bandwidth can also be increased. In general, the characteristic frequency (proportional to $I_C R_N$) of the junctions should be scaled up linearly with the synthesis frequency in order to avoid error in synthesized power due to nonideal pulse frequency response.

Finally, to achieve higher output frequencies, we can tune the diplexer filters and increase the $I_C R_N$ of the JJs to match the band of interest. Some potential multi-tone applications will also require the design of wider bandwidth stopband and passband filters. The layout of lumped-element filters beyond the simple second-order Butterworth design will be more feasible for higher design frequencies, because component feature sizes will be smaller.

VI. Conclusion

We have demonstrated pulse-based synthesis of gigahertz-frequency waveforms using arrays of Josephson junctions. We synthesized a sinusoidal waveform with −49 dBm power at 1 GHz and demonstrated a feedthrough-limited in-band SFDR of −79 dBc. These results were achieved by implementing a new bandpass-bandstop diplexer circuit that can be scaled in the future to synthesize waveforms with higher output power. Both the lumped-element RF-JAWS circuit and diplexer RF-JAWS circuit discussed in this article were designed to reduce error caused by feedthrough at the synthesis frequency; this feedthrough was shown to contribute approximately 4% error in both the measured lumped-element circuit and diplexer circuit output power. Quantum-locked operation of our circuits was verified, and the physical origin of trends in the fundamental tone power over the quantum-locked range were identified. These experimental results represent significant progress toward the goal of JAWS-synthesized quantum-based reference waveforms at gigahertz frequencies for calibration of RF electronics.

Acknowledgment

The authors thank the NIST Boulder Microfabrication Facility and the NIST staff who support it for fabrication of the superconducting JAWS chips described in this work. The authors also thank Dylan Williams, Jerome Cheron, and Alirio Boaventura for their contributed expertise in microwave design and signal calibration, as well as Ron Ginley and Kate Remley for their consultations on existing RF power calibration and waveform measurement techniques.

REFERENCES

[1] S. Benz and C. Hamilton, "A pulse-driven programmable Josephson voltage standard," *Appl. Phys. Lett.*, vol. 68, pp. 3171–3173, Jun. 1996.

[2] A. Rüfenacht, N. E. Flowers-Jacobs, A. E. Fox, C. J. Burroughs, P. D. Dresselhaus, and S. P. Benz, "Direct comparison of a pulse-driven Josephson arbitrary waveform synthesizer and a programmable Josephson voltage standard at 1 volt," in *Proc. Conf. Precision Electromagn. Meas.*, Jul. 2016, pp. 1–2.

[3] R. Behr, O. Kieler, J. Lee, S. Bauer, L. Palafox, and J. Kohlmann, "Direct comparison of a 1 V Josephson arbitrary waveform synthesizer and an ac quantum voltmeter," *Metrologia*, vol. 52, pp. 528–537, Jun. 2015.

[4] O. F. Kieler, R. Behr, R. Wendisch, S. Bauer, L. Palafox, and J. Kohlmann, "Towards a 1 V Josephson arbitrary waveform synthesizer," *IEEE Trans. Appl. Supercond.*, vol. 25, no. 3, Jun. 2015, Art. no. 1400305.

[5] J. A. Brevik, N. E. Flowers-Jacobs, A. E. Fox, E. B. Golden, P. D. Dresselhaus, and S. P. Benz, "Josephson arbitrary waveform synthesis with multilevel pulse biasing," *IEEE Trans. Appl. Supercond.*, vol. 27, no. 3, Apr. 2017, Art. no. 1301707.

[6] N. E. Flowers-Jacobs, A. E. Fox, P. D. Dresselhaus, R. E. Schwall, and S. P. Benz, "Two-volt Josephson arbitrary waveform synthesizer using Wilkinson dividers," *IEEE Trans. Appl. Supercond.*, vol. 26, no. 6, Sep. 2016, Art. no. 1400207.

[7] B. Jeanneret and S. Benz, "Application of the Josephson effect in electrical metrology," *Eur. Phys. J. Special Topics*, vol. 172, pp. 181–206, Jun. 2009.

[8] T. E. Lipe, J. R. Kinard, Y.-H. Tang, S. P. Benz, C. J. Burroughs, and P. D. Dresselhaus, "Thermal voltage converter calibrations using a quantum ac standard," *Metrologia*, vol. 45, no. 3, pp. 275–280, Jun. 2008.

[9] R. Toonen and S. Benz, "Nonlinear behavior of electronic components characterized with precision multitones from a Josephson arbitrary waveform synthesizer," *IEEE Trans. Appl. Supercond.*, vol. 19, no. 3, pp. 715–718, Jun. 2009.

[10] R. Lapuh, B. Volj, M. Lindi, and O. F. O. Kieler, "Keysight 3458A noise performance in DCV sampling mode," *IEEE Trans. Instrum. Meas.*, vol. 66, no. 6, pp. 1089–1094, Jun. 2017.

[11] D. Georgakopoulos, I. Budovsky, S. P. Benz, and G. Gubler, "Josephson arbitrary waveform synthesizer as a reference standard for the measurement of the phase of harmonics in distorted waveforms," *IEEE Trans. Instrum. Meas.*, vol. 68, no. 6, pp. 1927–1934, Jun. 2019.

[12] S. Bauer *et al.*, "A novel two-terminal-pair pulse-driven Josephson impedance bridge linking a 10 nF capacitance standard to the quantized Hall resistance," *Metrologia*, vol. 54, no. 2, pp. 152–160, Feb. 2017.

[13] F. Overney *et al.*, "Josephson-based full digital bridge for high-accuracy impedance comparisons," *Metrologia*, vol. 53, pp. 1045–1053, Jun. 2016.

[14] P. F. Hopkins *et al.*, "RF waveform synthesizers with quantum-based voltage accuracy for communications metrology," *IEEE Trans. Appl. Supercond.*, vol. 29, no. 5, Aug. 2019, Art. no. 1301105. [Online]. Available: https://ieeexplore.ieee.org/document/8638585/

[15] R. A. Ginley, "Traceability for microwave power measurements: Past, present, and future," in *Proc. IEEE 16th Annu. Wireless Microw. Technol. Conf.*, Apr. 2015, pp. 1–5.

[16] F. Clague, "A calibration service for coaxial reference standards for microwave power," NIST Technical Note 1374, May 1995.

[17] K. A. Remley, D. F. Williams, P. D. Hale, C. Wang, J. Jargon, and Y. Park, "Millimeter-wave modulated-signal and error-vector-magnitude measurement with uncertainty," *IEEE Trans. Microw. Theory Techn.*, vol. 63, no. 5, pp. 1710–1720, May 2015.

[18] D. Williams *et al.*, "Covariance-based uncertainty analysis of the NIST electrooptic sampling system," *IEEE Trans. Microw. Theory Techn.*, vol. 54, no. 1, pp. 481–491, Jan. 2006.

[19] K. A. Remley, "Multisine excitation for ACPR measurements," in *Proc. IEEE MTT-S Int. Microw. Symp. Dig.*, Jun. 2003, vol. 3, pp. 2141–2144.

[20] K. A. Remley, P. D. Hale, D. I. Bergman, and D. Keenan, "Comparison of multisine measurements from instrumentation capable of nonlinear system characterization," in *Proc. 66th ARFTG Microw. Meas. Conf.*, Dec. 2005, pp. 1–10.

[21] *Keysight E8663D PSG RF Analog Signal Generator—Data Sheet*, Keysight Technologies, Dec. 2017. [Online]. Available: https://literature.cdn.keysight.com/litweb/pdf/5990-4136EN.pdf

[22] R. Pintelon and J. Schoukens, *System Identification: A Frequency-Domain Approach*. New York, NY, USA: IEEE Press, 2001.

[23] F. Schaich and T. Wild, "Subcarrier spacing—A neglected degree of freedom?" in *Proc. IEEE 16th Int. Workshop Signal Process. Adv. Wireless Commun.*, Jun. 2015, pp. 56–60.

[24] T. S. Clement, P. D. Hale, D. F. Williams, C. M. Wang, A. Dienstfrey, and D. A. Keenan, "Calibration of sampling oscilloscopes with high-speed photodiodes," *IEEE Trans. Microw. Theory Techn.*, vol. 54, no. 8, pp. 3173–3181, Aug. 2006.

[25] C. J. Burroughs, S. P. Benz, P. D. Dresselhaus, and Y. Chong, "Precision measurements of ac Josephson voltage standard operating margins," *IEEE Trans. Instrum. Meas.*, vol. 54, no. 2, pp. 624–627, Apr. 2005.

[26] C. A. Donnelly, J. A. Brevik, P. D. Dresselhaus, P. F. Hopkins, and S. P. Benz, "Jitter sensitivity analysis of the superconducting Josephson arbitrary waveform synthesizer," *IEEE Trans. Microw. Theory Techn.*, vol. 66, no. 11, pp. 4898–4909, Nov. 2018.

[27] B. Baek, P. D. Dresselhaus, and S. P. Benz, "Co-sputtered amorphous Nb_x Si_{1-x} barriers for Josephson-junction circuits," *IEEE Trans. Appl. Supercond.*, vol. 16, no. 4, pp. 1966–1970, Dec. 2006.

[28] A. S. Boaventura, D. F. Williams, G. Avolio, and P. D. Hale, "Traceable characterization of broadband pulse waveforms suitable for cryogenic Josephson voltage applications," in *Proc. IEEE/MTT-S Int. Microw. Symp.*, Jun. 2018, pp. 1176–1179.

[29] WRSPICE circuit simulation software. Whiteley Research, Inc. [Online]. Available: www.wrcad.com

[30] T. V. Duzer, *Principles of Superconductive Devices and Circuits*, 2nd ed. Upper Saddle River, NJ, USA: Prentice Hall, 1998.

[31] F. Auracher and T. V. Duzer, "RF impedance of superconducting weak links," *J. Appl. Phys.*, vol. 44, no. 2, pp. 848–851, Jul. 1973.

[32] M. Maezawa, T. Yamada, and C. Urano, "Integrated quantum voltage noise source for Johnson noise thermometry," *J. Phys. Conf. Ser.*, vol. 507, May 2014, Art. no. 042023.

[33] J. A. Jargon, D. F. Williams, T. M. Wallis, D. X. LeGolvan, and P. D. Hale, "Establishing traceability of an electronic calibration unit using the NIST microwave uncertainty framework," in *Proc. 79th ARFTG Microw. Meas. Conf.*, Jun. 2012, pp. 1–5.

[34] P. Bhartia and P. Pramanick, *Modern RF and Microwave Filter Design*. Boston, MA, USA: Artech House, 2016.

[35] G. Matthaei, L. Young, and E. Jones, *Design of Microwave Filters, Impedance-Matching Networks, and Coupling Structures*. Norwood, MA, USA: Arctech House, 1980.

[36] M. Elsbury, "Broadband microwave integrated circuits for voltage standard applications," Ph.D. dissertation, University of Colorado, Boulder, CO, USA, May 2010.

[37] C. A. Donnelly*et al.*, "Quantized pulse propagation in Josephson junction arrays," *IEEE Trans. Appl. Supercond.*, to be published, doi: 10.1109/TASC.2019.2929481. [Online]. Available: https://ieeexplore.ieee.org/document/8770128

[38] A. Williams and F. Taylor, *Electronic Filter Design Handbook*, 2nd ed. New York, NY, USA: McGraw-Hill, 2006.